

Seasonally evolving hydraulic transmissivity beneath Greenland supraglacial lakes

Ching-Yao Lai (✉ cylai@ldeo.columbia.edu)

Columbia University

Laura Stevens

University of Oxford

Danielle Chase

Princeton University

Timothy Creyts

Columbia University

Mark Behn

Boston College

Sarah Das

Woods Hole Oceanographic Institution

Howard Stone

Princeton University <https://orcid.org/0000-0002-9670-0639>

Article

Keywords: Surface Meltwater, Ice Sheet Flow, Local Evolution of Drainage Systems, Surface Uplift Relaxation, Basal Hydrology

Posted Date: November 13th, 2020

DOI: <https://doi.org/10.21203/rs.3.rs-104092/v1>

License:  This work is licensed under a Creative Commons Attribution 4.0 International License.

[Read Full License](#)

Version of Record: A version of this preprint was published at Nature Communications on June 25th, 2021. See the published version at <https://doi.org/10.1038/s41467-021-24186-6>.

1 Seasonally evolving hydraulic transmissivity beneath Greenland 2 supraglacial lakes

3
4 Ching-Yao Lai¹, Laura A. Stevens², Danielle L. Chase³, Timothy T. Creyts¹, Mark D. Behn⁴, Sarah B.
5 Das⁵, Howard A. Stone³

6
7 1 Lamont-Doherty Earth Observatory, Columbia University, Palisades, NY, USA.

8 2 Department of Earth Sciences, University of Oxford, Oxford OX1 3AN, UK.

9 3 Department of Mechanical and Aerospace Engineering, Princeton University, Princeton, NJ, USA.

10 4 Department of Earth and Environmental Sciences, Boston College, Chestnut Hill, MA, USA

11 5 Department of Geology and Geophysics, Woods Hole Oceanographic Institution, Woods Hole, MA,
12 USA.

13
14 *Ching-Yao Lai (cylai@ldeo.columbia.edu)

16 **Abstract**

17 Surface meltwater reaching the base of the Greenland Ice Sheet transits through drainage
18 networks, modulating the flow of the ice sheet. Dye-tracing studies indicate that drainage
19 efficiency evolves seasonally along the drainage pathway. However, the local evolution of
20 drainage systems further inland, where ice thicknesses exceed 1000 m, remains largely unknown.
21 Here, we develop a novel method to infer transmissivity of the drainage system based on surface
22 uplift relaxation following rapid lake drainage events. Combining field observations of five lake
23 drainage events with a mathematical model and laboratory experiments, we show that the surface
24 uplift decreases exponentially with time, as the water in the blister formed beneath the drained
25 lake permeates through the subglacial drainage system. This deflation obeys a universal
26 relaxation law with a timescale that reveals hydraulic transmissivity and indicates a two-order-
27 of-magnitude increase in subglacial transmissivity as the melt season progresses, suggesting
28 significant changes in basal hydrology beneath the lakes.

32 **Main Text**

33 Thousands of supraglacial lakes form annually on the surface of the Greenland Ice Sheet in
34 response to seasonal melt that fills topographic depressions. Many of these lakes drain rapidly
35 (<1 day), transporting meltwater through vertical hydrofractures directly to the ice-bed interface
36 (2, 6, 13). Surface meltwater entering the subglacial drainage system at the ice-bed interface
37 plays crucial roles in modulating the flow of the Greenland Ice Sheet (1–6). As the melt season
38 progresses, observations and theories suggest that the basal hydrologic system beneath the
39 Greenland Ice Sheet transitions from an inefficient distributed network to a more efficient
40 channelized system that transmits more water at lower pressure (7–10). Drainage type, whether
41 distributed or channelized, impacts basal sliding and ice discharge (3, 8–10).

42

43 Understanding the degree and the spatial extent of the drainage system transition is paramount
44 for characterizing sliding during the melt season. Field-based dye tracer studies in ice sheet
45 marginal regions (7, 8) suggest a progressive channelization throughout the melt season and
46 indicate that Greenland Ice Sheet hydrology undergoes a 5-fold increase in subglacial water
47 speed as a channelized system develops near the terminus (8). However, the effect of
48 channelization tapers at higher elevations (>1000 m above sea level [a.s.l.]) (11, 44), where
49 evolution of local basal hydrology remains poorly constrained by observations. Furthermore,
50 observational-based estimates for hydraulic transmissivity, a key parameter controlling the water
51 discharge in a subglacial sheet under the ice sheet for a given hydraulic potential gradient, are
52 scarce. Here we probe the evolution of local hydraulic transmissivity (10, 12) beneath rapidly
53 draining supraglacial lakes (1000–1350 m a.s.l.) using a new method combining field
54 observations, a mathematical model, and laboratory experiments.

55

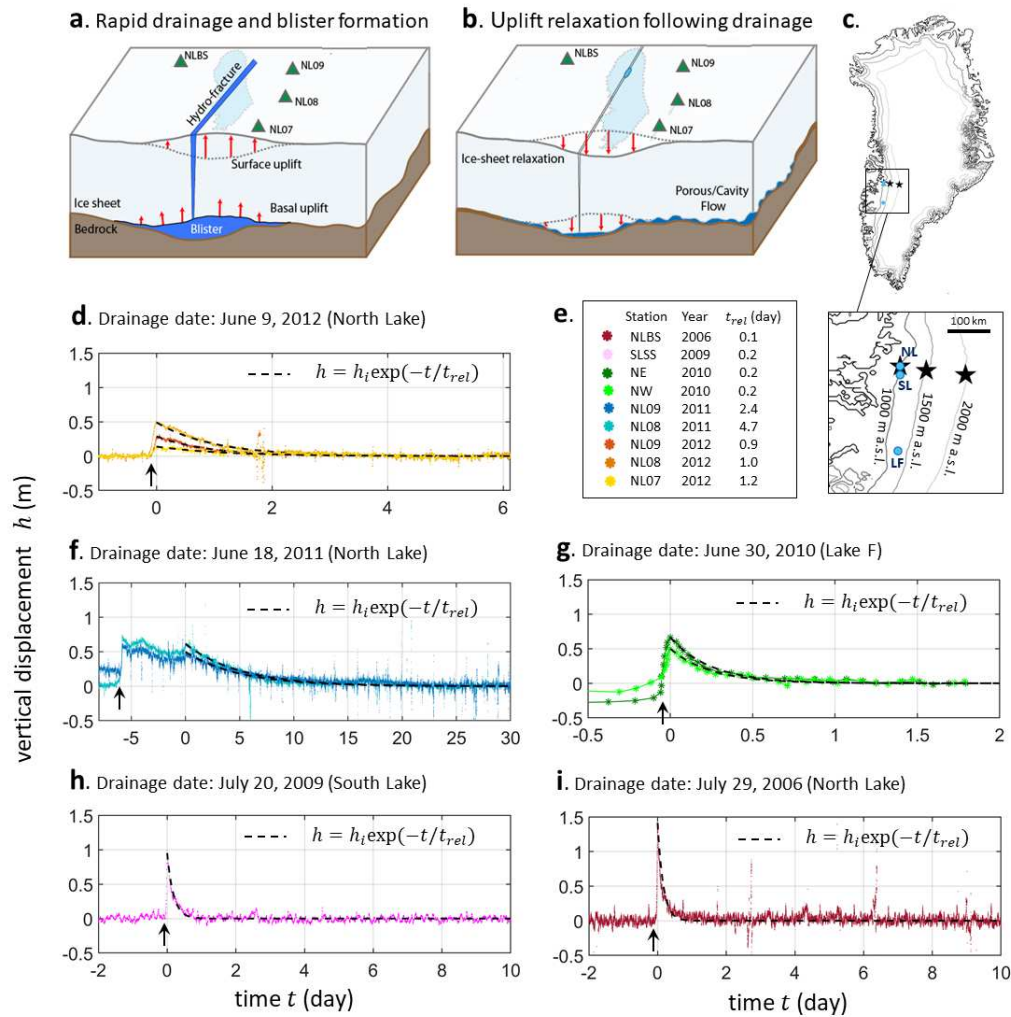
56 **Results**

57 **Relaxation of surface uplift following lake drainage**

58 Rapid drainage of lakes injects surface meltwater into the ice-bed interface. The water can be
59 transiently stored in water-filled “blisters” (Fig. 1a) that lift and deform the overlying ice sheet
60 (4, 6, 13, 14). After a lake drainage event, surface uplift decays over time (2) as water exits the

61 blister and spreads along the ice-bed interface (Fig. 1b). Previous studies have documented the
 62 initial stages of lake drainage and blister formation (2, 6) and modeled the effect of lake drainage
 63 on the subglacial hydrological system (11). Here we focus on the long-term surface relaxation
 64 (1–10 days) of the ice sheet after a lake drains to quantify the hydraulic transmissivity (10, 12) of
 65 the surrounding subglacial drainage system.

66



67

Fig. 1. Ice-sheet uplift relaxation following rapid supraglacial lake drainage. Schematic drawings of the North Lake GPS array that observes ice-sheet surface uplift and speed (a) during subglacial blister formation at the time of rapid drainage, and (b) post-drainage relaxation as the blister drains into the surrounding ice-bed interface. (c) The locations of North Lake (NL), South

Lake (SL), and Lake F (LF) are marked by the blue dots. The star at 1000 m a.s.l. is the North Lake location. (d–i) Ice-sheet surface elevation during rapid drainage (drainage start time marked by arrows) and post-drainage uplift relaxation from GPS stations for five different drainages, where post-drainage uplift relaxation begins at time = 0 days. Dashed curves show vertical displacement data fit to the exponential function, $h(t) = h_i \exp(-t/t_{rel})$. The fitted t_{rel} , the lake drainage year, and the station name for each GPS station are listed in the table in e. The two uplift peaks following the 2011 drainage shown in panel f likely result from additional water injection into the blister from nearby surface or basal sources (6). For the 2011 data, we therefore set time zero to be the time after which uplift only relaxes, and no significant amounts of additional water enter the blister.

68

69 Using ice-sheet surface elevation data from on-ice GPS stations, we characterize the relaxation
70 timescale for five lake drainage events from three separate lakes along the western margin of the
71 Greenland Ice Sheet (Fig. 1d-i; Supplementary Table 1). The five rapid lake drainages have
72 drainage dates that span from the early melt season (typically May through June) through the late
73 melt season (typically July through September). We find a wide range of relaxation timescales of
74 surface uplift (from 12 hours to 10 days) depending on when lake drainage occurs within the
75 melt season (Fig. 1d-i). Ice-sheet surface uplift relaxation is fitted by an exponential function
76 (dashed curves in Fig. 1d-i and Supplementary Fig. 4f-j) to quantify the relaxation time t_{rel} . We
77 set time zero to be the time at which uplift begins to relax continuously back to pre-drainage
78 values. Larger relaxation times t_{rel} are generally observed for drainages that occur earlier in the
79 melt season (e.g., North Lake 2006 (Fig. 1i)) and smaller t_{rel} are observed for drainages later in
80 the melt season (e.g., North Lake 2011 (Fig. 1f)).

81

82 **Blister relaxation model**

83 Relaxation of surface uplift following a lake drainage event can be explained by gradual drainage
84 of the blister into the neighboring subglacial drainage system (Fig. 1b). Based on this conceptual
85 model we hypothesize that the relaxation timescales are controlled by the subglacial drainage
86 system beneath the ice sheet. To test this hypothesis, we develop a model that links the surface
87 relaxation to the hydraulic transmissivity of the drainage system.

88

89 Near the ice-sheet margin the subglacial drainage system is thought to evolve seasonally (3, 7-
 90 10) from an inefficient, distributed drainage system early in the melt season to an efficient,
 91 channelized system later in the melt season. However, an analogous shift in drainage style has
 92 not been observed at higher elevations (8, 11). At elevations where supraglacial lakes form
 93 (~1000 m a.s.l.), subglacial hydrological models indicate that water discharge remains in a
 94 distributed network after a lake drainage event (11). Models indicate that short, discontinuous
 95 channels form following lake drainage, but these channels do not significantly affect subglacial
 96 water pressure or discharge (11). Field evidence (8) also suggests that channels do not develop
 97 until early August in 1000 m a.s.l. regions (Supplementary Table 1). Based on these
 98 observations, we assume a distributed drainage model to simulate surface uplift relaxation after
 99 the five lake drainage events (June and July; Supplementary Table 1).

100

101 Uplift relaxation is driven by the elastic deformation of ice lying above the water-filled blister
 102 and resisted by the viscous dissipation of the water flow in the distributed drainage system.
 103 Below we use scaling arguments to obtain a characteristic timescale of blister relaxation t_c . The
 104 full mathematical model for blister relaxation dynamics is detailed in Supplementary Information
 105 Section 1.

106

107 For a blister of maximum thickness H and radius R (Fig. 2a) the blister volume scales as $V \approx$
 108 $2\pi\alpha HR^2$ (equation (S.15)), where α is a dimensionless parameter related to the shape of the
 109 blister. From mass conservation, the blister volume relaxation rate ($dV/dt \approx V/t_c$) equals the
 110 water flux entering the distributed water sheet of depth h_0 and porosity ϕ (ratio between pore
 111 space to total space) with flow velocity u_p (red arrows in Fig. 2a) at radial distance r . Thus, a
 112 mass balance yields (see equations (S.12) and (S.15))

$$113 \quad \frac{V}{t_c} \approx \frac{2\pi\alpha HR^2}{t_c} \approx r\phi u_p h_0 \quad (1)$$

114 Drainage rules based on Darcy's law for flow in porous materials have been used for numerous
 115 types of distributed drainage morphologies, such as films (15–17), linked cavities (18, 19), and
 116 porous sediment sheets (20). The key feature shared by these distributed systems is that the water

117 flux $\phi \mathbf{u}_p$ (volume per time per unit area crossing the flow) increases linearly with the gradient of
 118 water pressure p . Thus, distributed systems can be modeled as a water sheet with an effective
 119 permeability k that obeys Darcy's law $\phi \mathbf{u}_p = -\frac{k}{\mu} \nabla p$, where μ is water viscosity. Note that in
 120 both field data and our laboratory experiments the blister radius R remains unchanged during
 121 blister relaxation (Fig. 2c) and is assumed constant in our model. We estimate that the horizontal
 122 viscous pressure drops in the water sheet and the blister for $r < R$ are negligibly small
 123 (Supplementary Information Section 1.5) compared with the viscous pressure drop Δp_v in the
 124 water sheet at $r > R$. Integrating the pressure gradient radially along the water sheet over $r >$
 125 R and considering mass conservation, we obtain a horizontal pressure drop (equation (S.18)) of
 126 magnitude

$$127 \quad \Delta p_v \approx \frac{\mu}{h_0 k} \frac{V}{t_c} \ln \left(\frac{R_p}{R} \right), \quad (2)$$

128 where R_p is the radius of the invading water front in the water sheet.

129

130 Deformation of the ice overlying the blister generates elastic stresses in the ice sheet. For a
 131 penny-shaped blister (13, 21–23), the magnitude of the elastic stresses in ice can be estimated by
 132 Hooke's law corresponding to an approximate strain H/R (see equation (S.16)):

$$133 \quad \Delta p_e \approx \frac{EH}{2(1-\nu^2)R} \quad (3)$$

134 For a typical blister radius $R \approx 2$ km and maximum thickness $H \approx 1$ m, and ice with Young's
 135 modulus $E \approx 10$ GPa and Poisson's ratio $\nu \approx 0.3$, the elastic stress is $\Delta p_e \approx 2$ MPa. The elastic
 136 stresses caused by the blister are balanced by an increase in water pressure in addition to the
 137 hydraulic potential. Thus, the water pressure in the blister at the base of a uniform ice sheet of
 138 thickness $d \approx 1$ km is $p = \rho_i g d + \rho_w g h + \Delta p_e$ (equation (S.38)), where $h(r, t)$ is the water
 139 thickness in the blister, ρ_w and ρ_i are the water and ice density, respectively, and g is the
 140 gravitational acceleration. Subglacial flow is driven by the water pressure gradient ∇p , where the
 141 gradient of ice and water overburden pressure are negligible compared with that of the elastic
 142 stress (Supplementary Information Section 2). Thus, during ice-sheet relaxation the elastic

143 stresses, rather than the ice and water overburden pressure, dominantly drive subglacial flow and
 144 blister relaxation.

145

146 The relaxation dynamics are governed by a balance between the elastic stresses Δp_e driving the
 147 relaxation and the pressure drop Δp_v resisting the subglacial flow, i.e., $\Delta p_e \approx \Delta p_v$. Thus,

148 equations (1-3) give the characteristic relaxation time $t_c = 4\pi\alpha \ln(R_p/R)\mu R^3 (1 -$
 149 $v^2)/(Ekh_0)$. Neglecting the constants of order-magnitude one (e.g., π) and the numerical pre-

150 factor $\alpha \ln\left(\frac{R_p}{R}\right) \approx f = O(1)$ (equation (S.26)) that do not affect the scaling, we obtain the

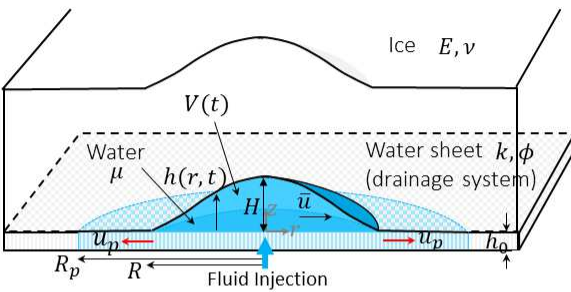
151 characteristic relaxation time:

$$152 \quad t_c = \mu R^3 (1 - v^2)/(Ekh_0) \quad (4)$$

153 This timescale will be used to rescale the experimental and field data.

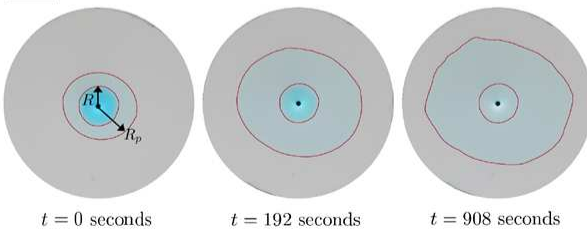
154

a. Blister Model

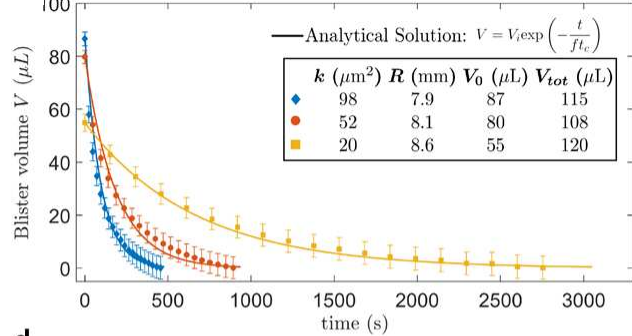


b.

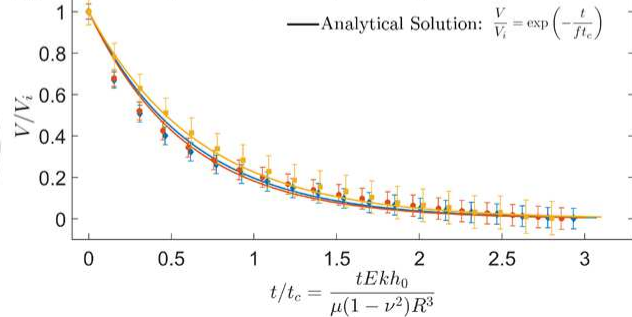
2 cm



c.



d.



155

Fig. 2. Experimental validation of the mathematical model. (a) Schematic of the blister model. An elastic layer (ice) with Young's modulus E and thickness d over a porous substrate (drainage system) of thickness h_0 , porosity ϕ , and permeability k . Injection of a liquid with volume V_{tot} and viscosity μ into the interface between the elastic layer and the substrate forms a blister. The experimental parameters are listed in Supplementary Table 3. (b) The top view of the experimental relaxation dynamics, during which liquid in the blister (dark blue) enters the pore space (light blue), increasing fluid area in the porous substrate. The blister and the fluid front in the porous substrate are outlined. During relaxation the blister radius R remains approximately constant. Since $t_c \propto R^3$ via equation (4), the laboratory relaxation time ($\sim 10^3$ seconds) of a laboratory-scale blister ($R \sim 10$ mm) is expected to be much shorter than that observed in the field. (c) Measured blister volumes $V(t)$ for three different substrate permeabilities decrease exponentially with time. Experimental parameters are listed in Supplementary Table 3. The analytical solution is given by equation (6). (d) The dimensionless experimental data fall onto a common curve, agreeing well with the exponential solution (equation (6) with $f = 0.6 - 0.7$ (Supplementary Table 3); solid curves).

156

157 Considering mass conservation and a force balance analysis (Supplementary Information Section
158 1), we obtain a nonlinear ordinary differential equation for the blister volume $V(t)$:

$$159 \quad \frac{E}{1(1-\nu^2)} \frac{V}{2\alpha\pi R^3} + \frac{\mu}{4\pi h_0 k} \ln\left(\frac{V_{tot}-V}{\phi\pi h_0 R^2}\right) \frac{dV}{dt} = 0, \quad (5)$$

160 where V_{tot} is the total volume of water in the system. Equation (5) can be solved numerically and
161 approximated by a linear ordinary differential equation ((Supplementary Information Section 1;
162 equation (S.25)), yielding exponential solutions for the blister volume $V(t)$ and thickness $h(r, t)$
163 as a function of time t and radial distance r :

$$164 \quad V(t) = V_i \exp\left(-\frac{t}{ft_c}\right) \quad (6)$$

$$165 \quad h(r, t) = h_i(r) \exp\left(-\frac{t}{ft_c}\right), \quad (7)$$

166 where $V_i = V(t = 0)$, $h_i(r) = h(r, t = 0)$, and f is a numerical pre-factor (equation (S26)).
167 Comparing equation (7) with $h(t) = h_i \exp(-t/t_{rel})$ gives $f = t_{rel}/t_c$. The analytic
168 approximation is in close agreement to the numerical solution (Supplementary Fig. 1) The

169 relaxation dynamics are negligibly impacted by the bed slope (Supplementary Information
170 Section 2) and the melting and viscous motion of ice (Supplementary Information Section 3).

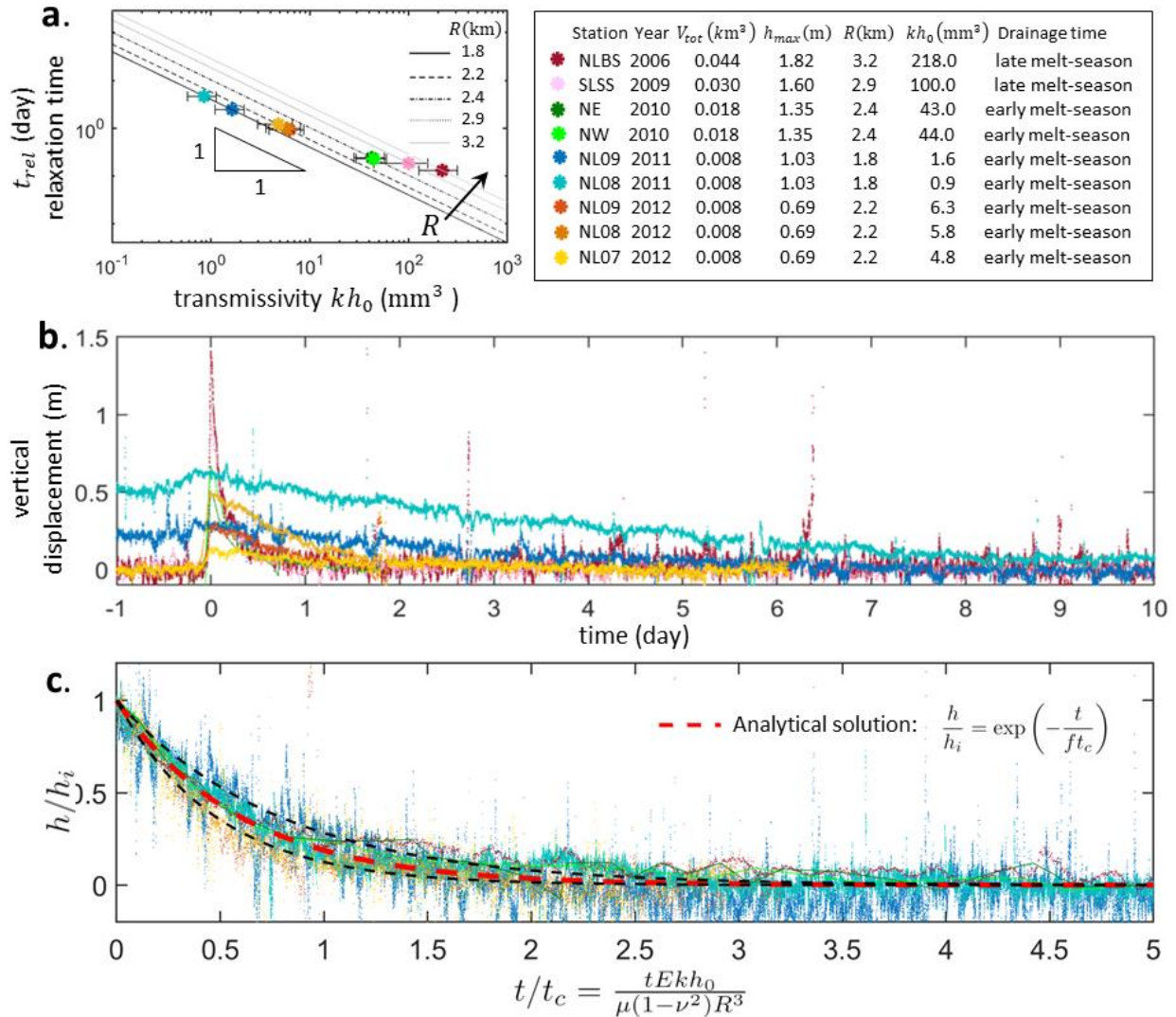
171
172 Based on field observations and lab experiments, we assume R is constant so that the only way
173 for blister volume to decrease is pushing water through the porous water sheet, yielding an
174 exponential decay of blister height. In contrast, Hewitt et al. (2018) (14) considered a blister
175 propagating on a water-filled porous sheet with an increasing R and decreasing h . In their model,
176 water volume in the blister V is constant and does not leak into the porous water sheet, resulting
177 in a power-law decrease of blister height as a function of time (14). A comparison of the GPS
178 uplift data with the power-law decay (14) and our exponential decay (equation (7)) is shown in
179 Supplementary Fig. 7. The GPS uplift data exhibits better agreements with our exponential
180 solutions.

181 182 **Laboratory experiments**

183 Next, we tested the analytic model (equations (4) and (6)) against our laboratory experiments,
184 which allow precise control and direct measurement of sheet permeability. Experiments on fluid
185 peeling between an elastic sheet and a non-permeable rigid substrate have previously been
186 investigated (45). In contrast, here we consider a porous substrate that mimics the distributed
187 drainage system. In our experiment, a fluid-filled blister (dark blue in Fig. 2b) is generated via
188 liquid injection into the interface between a transparent elastic layer and a porous substrate. This
189 setup mimics ice lying above a distributed drainage system (Fig. 2a). After injection of liquid,
190 the fluid permeates from the blister through the porous substrate (light blue in Fig. 2b), the blister
191 thickness decreases and the blister radius remains unchanged, which differs from the increasing
192 R in Hewitt et al. (2018) (14). Our lab experiments show that varying the permeability of the
193 porous substrate k significantly impacts the relaxation timescale in the experiments (Fig. 2c).
194 The blister volume $V(t)$ relaxes exponentially with time, validating our analytical solution
195 (equation (6), curves in Fig. 2c). All parameters in the analytical solution can be calculated based
196 on the experimental variables except for the pre-factor f (Supplementary Table 3). After
197 rescaling the blister volume V with V_i and time t with t_c (equation (4)), the experimental data for

198 different permeabilities collapse onto a universal curve (Fig. 2d), demonstrating the model's
 199 success in predicting the impact of permeability on the relaxation timescale.

200



201

Fig. 3. Hydraulic transmissivity and the universal dynamics of uplift relaxation. (a) The relaxation time t_{rel} obtained from surface uplift data from different stations and the predicted hydraulic transmissivity kh_0 . The detailed information for each data set is shown in the table. Here the supraglacial lake volume is assumed to be the total volume V_{tot} injected into the blister and the water sheet. The black lines ($t_{rel} = f \frac{\mu R^3(1-\nu^2)}{E} (kh_0)^{-1}$) are the model predictions for different

blister radii R . The lake volume V_{tot} of Lake F and North Lake listed in the table are taken from references (2, 4, 6) and lake volume of South Lake is estimated in Methods. Surface uplift data from five drainages of three different lakes as recorded by seven different stations are plotted in (b) dimensional and (c) dimensionless forms. Despite a wide range of relaxation times, when rescaled by the characteristic relaxation time t_c (equation (4)) and initial vertical displacement h_i , all field uplift data collapse onto the exponential analytical solution (equation (7), red dashed line (panel c) with $f = 0.6$ averaged over all datasets (Methods)). Upper and lower dashed lines represent the solutions with the highest and lowest f , respectively, among all the data sets.

202

203 **Inferring hydraulic transmissivity from surface GPS data**

204 We then applied the validated model to estimate hydraulic transmissivity kh_0 (12) of the
 205 subglacial water sheet from surface uplift data following the five lake drainage events
 206 (Supplementary Table 1). The relaxation time t_{rel} of each set of GPS data was obtained by
 207 fitting $h(t) = h_i \exp(-t/t_{rel})$ (dashed curves in Fig. 1) to the GPS data. According to equation (4)
 208 and $f = t_{rel}/t_c$, the hydraulic transmissivity can be expressed as $kh_0 = \frac{\mu R^3(1-\nu^2)}{Et_c} = f \frac{\mu R^3(1-\nu^2)}{Et_{rel}}$
 209 (lines in Fig. 3a) and calculated using the relaxation time t_{rel} , the Young's modulus of ice E ,
 210 water viscosity μ , Poisson's ratio ν , blister radius R estimated from the lake volume V_{tot}
 211 (Methods), and the pre-factor $f = O(1)$ (equation (S.26); Supplementary Table 3). This
 212 transmissivity estimate is valid within a 2–6 km horizontal distance (the extent of water in the
 213 sheet displaced by the lake volume) from the lake-drainage location. The transmissivity
 214 estimated for each lake drainage event based on the GPS uplift data is shown in Fig. 3a and
 215 Supplementary Table 3. Note that the variability of the transmissivity estimated from different
 216 stations for the same drainage event is less than that between different drainage events. The
 217 uncertainties propagated in the transmissivity estimate are reported in Supplementary Table 2
 218 (Methods).

219

220 **Universal uplift relaxation dynamics**

221 To demonstrate the universality of the time-dependent uplift relaxation data, we rescaled the
 222 surface uplift data (Fig. 3b) by the characteristic relaxation time t_c , as calculated from Equation

223 (4) using the parameters listed in Fig. 3a, and the initial vertical displacement h_i . The rescaled
224 data collapse (Fig. 3c) onto the analytical solution, equation (7). Thus, despite variability in local
225 lake basin and ice-sheet bed geometry, surface uplift magnitude, and timescale of uplift
226 relaxation, the collapse of the data onto a universal curve indicates that the relaxation dynamics
227 depends to first order on two dimensionless parameters, h/h_i and t/t_c .

228

229 **Seasonal evolution of transmissivity under supraglacial lakes**

230 Finally, we compare the transmissivities for lakes draining at different times in the melt season.
231 Our results suggest the local transmissivity of the basal drainage system beneath North Lake can
232 evolve by up to two orders of magnitude over the melt season. Early-season events relax more
233 slowly as characterized by a low-transmissivity drainage system ($kh_0 = O(1) \text{ mm}^3$). By
234 contrast, the late-season events relax faster and are best explained by high transmissivity ($kh_0 =$
235 $O(10^2) \text{ mm}^3$). When comparing our estimates of hydraulic transmissivity to modeled cumulative
236 surface runoff (27) at the time of lake drainage, we observe that transmissivity generally
237 increases with increased cumulative runoff (Fig. 4a). Our results suggest that local transmissivity
238 beneath draining lakes at ~ 1000 m a.s.l. increases by up to two orders of magnitude throughout
239 the melt season correlating to the cumulative volume meltwater moving through the system (Fig.
240 4a). Comparing the range of transmissivity values we obtained from the field data ($kh_0 = O(1 -$
241 $10^2) \text{ mm}^3$) with the hydraulic conductivity (24) used in large-scale hydrological models (11)
242 ($K \equiv \frac{k\rho_w g}{\mu} \approx 0.05 - 0.5 \text{ m s}^{-1}$), we calculate that the sheet depth is of order $h_0 = O(10^{-1} - 1)$
243 m. All parameters used in the transmissivity calculation are listed in Supplementary Table 3.

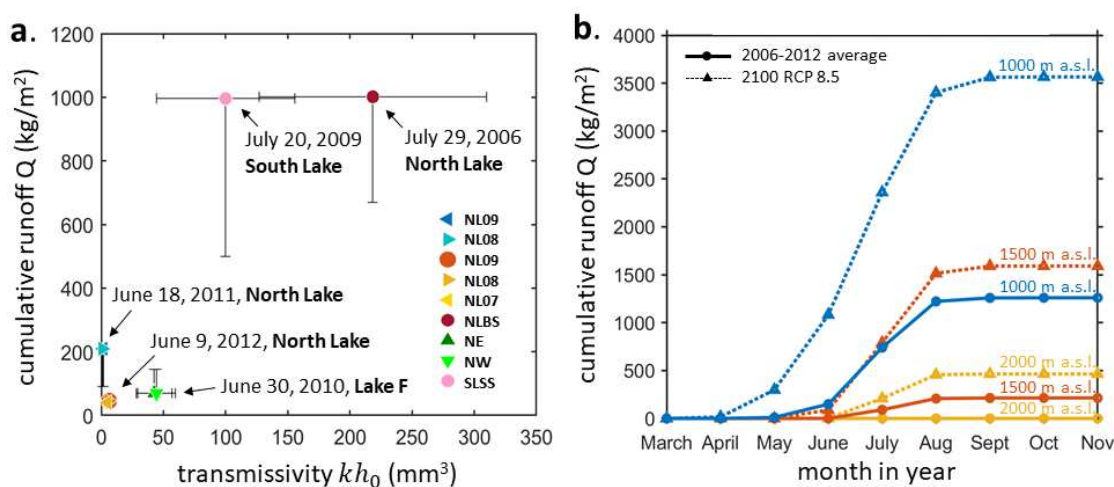
244

245 **Discussion**

246 We infer that local hydraulic transmissivity under North Lake (~ 1000 m a.s.l.) evolves
247 seasonally. Our method can be applied to estimate local transmissivity beneath other draining
248 supraglacial lakes simply based on surface observation of uplift and lake volume. Dye tracer
249 experiments have the advantage of tracking subglacial water speed at different times of the year,
250 which well characterize the evolution of subglacial efficiency near the marginal areas. However,

251 it is challenging to use dye tracing experiments to gauge the evolution of drainage systems near
 252 higher-elevation regions (>1000 m a.s.l.; far away from the ice-sheet margin). Although a dye
 253 tracing experiment was done at a moulin near 1000 m a.s.l. (moulin L41 in Chandler et al
 254 (2013)), the measured water velocity was averaged along a 41-km-long water pathway (8). Thus,
 255 it is unclear if the drainage system actually evolves near 1000 m a.s.l., because channelization
 256 near the margins would also cause an increase in observed tracer velocities. Our results show
 257 evidence that the drainage system evolves locally at the lake elevations (~1000 m a.s.l.). In
 258 addition, dye tracer experiments are limited to sampling moulines in land-terminating glaciers
 259 located mainly in south-west Greenland. By contrast, supraglacial lakes are widespread over the
 260 ice sheet, forming in progressively higher elevation regions as the climate warms (28).

261



262

Fig. 4. Seasonal variation of hydraulic transmissivity. (a) Transmissivity inferred from five drainage events across three lakes as a function of cumulative runoff. Cumulative runoff is the sum of daily, 11-km resolution RACMO runoff estimates (27) from the first day of the year up to the drainage date at the nearest RACMO grid cell to the drainage location (Methods). (b) Time evolution of cumulative runoff (monthly output) obtained from the regional climate model MAR averaged from 2006 to 2012 (solid curves) and its 2100-projections under the RCP 8.5 scenario (29) (dashed curves), evaluated at the three locations (elevations) marked as stars in Fig. 1c.

263

264 Quantifying hydraulic transmissivity of high-elevation areas (>1000 m a.s.l.) is crucial for
265 understanding ice-sheet behavior in a warming climate. Our method provides an approach to
266 determine the magnitude and seasonal evolution of transmissivity of high-elevation regions using
267 only observations of surface deformation and lake volume. Under RCP scenario 8.5 (29), total
268 melt season runoff at 1500 m a.s.l. in 2100 is projected to be higher than the average total melt
269 season runoff from 2006–2012 observed at North Lake (~1000 m a.s.l.) (Fig. 4b). Thus, over the
270 coming decades as runoff increases and surface-to-bed meltwater pathways migrate inland to
271 higher elevations (30), we expect an overall increase in transmissivity in the ice-sheet interior.
272 Such an increase would likely impact the timescale of sliding in response to meltwater accessing
273 the bed in ways not currently considered in the basal sliding law (10). Indeed, we observe the
274 transient ice flow velocities remain elevated over a shorter time period for high-transmissivity
275 drainage systems (Supplementary Fig. 6a-b), compared to a less efficient bed drainage
276 (Supplementary Fig. 6c-d). To date, no observations of transmissivity exist for elevations above
277 the five lakes investigated in this study. Such observations are needed to constrain processes
278 governing the future evolution of sliding in the ice-sheet interior.

279

280

281

282

283

284

285

286

287

288

289

290 **Materials and Methods**

291 **1 Field Data**

292 **1.1 GPS**

293 Continuous 30-s resolution GPS data collected by dual-frequency Trimble NetR9 receivers were
294 processed with Track software (31). GPS data for each station were processed individually
295 relative to the 30-s resolution Greenland GPS Network (GNET) KAGA base station located on
296 bedrock, 55 km from North Lake (32). $1-\sigma$ error output from Track software for these data are
297 the order of ± 2 cm in the horizontal and ± 5 cm in the vertical across all stations and years (6).
298 GPS data are archived at UNAVCO (see Data and materials availability).

299

300 **1.2 Uplift Data Processing**

301 The vertical displacement of each GPS station shows trends related to background ice sheet
302 advection through the lake basins. For example, in Supplementary Fig. 4a-e the background
303 vertical displacement $y(t)$ slowly varies with time t before and after the uplift peak caused by
304 the 5 lake drainage events. These background trends are fitted to a linear model ($y = at + b$,
305 where a, b are constants) and subtracted to yield the detrended vertical displacement $h(t)$
306 (Supplementary Fig. 4f-j, also plotted in Fig. 1d-i). When fitting the relative vertical
307 displacement to the linear model, we avoid the peak caused by lake drainage. For consistency,
308 we fit the linear model to the relative vertical displacement data, terminating at time t_{end} (the
309 right end of each plot in Supplementary Fig. 4), after the peak during $t_{end}/2 < t < t_{end}$ and
310 before the peak during $-t_{end}/4 < t < 0$, as shown by the black lines in Supplementary Fig. 4a-
311 b,e. For the 2011 data (Supplementary Fig. 4d) there are two uplift peaks after lake drainage,
312 likely caused by additional water injected by nearby sources, thus the data during the first peak is
313 avoided in the fitting of the linear model. The uplift data for Lake F (Supplementary Fig. 4c) is
314 obtained from Fig. 6e,h in Doyle et al. (2013) (4). Since Lake F data is sparse and not available
315 for a longer time span, we simply subtract the data from its final vertical position (0.3 m and 0.2
316 m for stations NW and NE, respectively; Supplementary Fig. 4h). After detrending, the reference
317 vertical displacements for all data sets are zero.

318

319 The detrended vertical displacements $h(t)$ for $t > 0$ (Supplementary Fig. 4f-j) are then fitted to
320 an exponential curve [$h(t) = h_i \exp(-t/t_{rel})$, where h_i is the initial displacement at time zero;
321 dashed curves in Supplementary Fig. 4f-j] to give the relaxation time t_{rel} used for this study
322 (vertical axis in Fig. 3a).

323

324 **1.3 South Lake 2009 Drainage and Volume**

325 Previous work has detailed multiple rapid drainages of North Lake (2, 6, 33, 34). Vertical and
326 horizontal ice-sheet surface displacements and lake drainage volumes have not been previously
327 detailed for South Lake (68.57° N, 49.37° W) (Supplementary Fig. 5a). South Lake is located at
328 1050 m above sea level (a.s.l.) on the western margin of the Greenland Ice Sheet, roughly 22 km
329 south of North Lake (33, 35).

330

331 In 2009, South Lake rapidly drained on July 20, 2009, as indicated by uplift of GPS station SLSS
332 (Supplementary Fig. 5b). No additional GPS were deployed in the vicinity of South Lake with a
333 temporal sampling resolution adequate to observe the rapid drainage event in 2009. Ice-sheet
334 vertical and horizontal displacements following the 2009 drainage of South Lake are most
335 similar to the 2006 rapid drainage of North Lake (Supplementary Fig. 5a). SLSS station attains
336 an uplift of 0.93 m over the initial 1.2 hours of the drainage event, before relaxing to its pre-
337 drainage elevation over the following ~14 hours (Supplementary Fig. 5b). SLSS depicts a pre-
338 drainage along-flow velocity of 141.7 m yr⁻¹, and a duration of 2.05 days is observed between
339 the time of lake drainage and the time of along-flow displacement attaining the displacement
340 predicted by pre-drainage along-flow velocities (Supplementary Fig. 5b).

341

342 The 30-m resolution MEaSUREs Greenland Ice Mapping Project (GIMP) Digital Elevation
343 Model (DEM) from GeoEye and WorldView Imagery, Version 1 (36, 37) and Landsat 7 imagery
344 were used to estimate the pre-drainage volume of South Lake. The last available image of South
345 Lake in 2009 was taken on July 15, 2009, five days prior to South Lake's rapid drainage

346 (Supplementary Fig. 5a). The lake margin on July 15, 2009 was mapped (Supplementary Fig. 5a)
347 and used to compare to elevation contours of South Lake from the GIMP DEM (Supplementary
348 Fig. 5b). The region of the GIMP DEM covering South Lake was created with a WorldView
349 image taken on July 17, 2012 (36), at which time South Lake basin did not host a lake, as South
350 Lake drained on or before June 12, 2012 based on the Landsat image archive. Therefore, while
351 there could be elevation changes between 2009 and 2012, the GIMP DEM over South Lake
352 depicts a dry lake basin.

353

354 Based on a comparison between the mapped South Lake margin and GIMP DEM elevation
355 contours, the South Lake margin elevation was estimated to be 1050.5 m a.s.l. (Supplementary
356 Fig. 5b), yielding a lower bound on the lake volume estimate for South Lake of 0.029 km^3 , with
357 maximum lake depths on the order of 10--15 m (Supplementary Fig. 5c). The GIMP DEM
358 reports a 1σ error of ± 1.27 m for every elevation estimate in the South Lake area
359 (Supplementary Fig. 5b). A $\pm 1\sigma$ error on the estimated lake margin elevation of 1050.5 m a.s.l.
360 (Supplementary Fig. 5b) yields a lake volume error of 0.006 km^3 . This error estimate should
361 presumably be a bit larger ($\sim 0.01 \text{ km}^3$), given the GIMP DEM time stamp is in 2012, and the
362 last pre-drainage image of South Lake was taken 4 days before the 2009 drainage. Following this
363 methodology, we estimate the 2009 South Lake drainage volume to be $0.03 \pm 0.01 \text{ km}^3$.

364

365 **1.4 Uncertainties in Estimating Model Parameters**

366 The error bars of transmissivity kh_0 in Fig. 3a result from uncertainties in estimating (1) lake
367 volume V_{tot} , (2) maximum blister height at the beginning of lake drainage h_{max} , and (3) blister
368 radius R . The uncertainties associated with the three parameters are listed in Supplementary
369 Table 2 and detailed below.

370

371 **1.4.1 Lake volume.** The lake volume V_{tot} and its measurement errors for 2009 North Lake,
372 2010 Lake F, 2011 and 2012 North Lake are reported in Das et al. (2008) (2), Doyle et al. (2013)
373 (4), Stevens et al. (2013) (6), respectively. The estimate uncertainty for 2006 South Lake volume

374 is detailed in Methods (section 1.3). The lake volume values are listed in the table in Fig. 3 with
375 error bars listed in Supplementary Table 2.

376

377 **1.4.2 Maximum blister height.** The maximum blister height h_{max} for all drainage events are
378 listed in the table in Fig. 3 with uncertainties listed in Supplementary Table 2. For 2011 and 2012
379 drainage events, h_{max} are available from the Network Inversion Filter (NIF) (38) algorithm in
380 Stevens et al. (2015) (6), which solves for the blister height based on surface displacement data
381 from a network of 15 GPS stations around the blister at North Lake. The NIF calculation is not
382 performed for 2006, 2009, and 2010 drainage events because there are not enough nearby GPS
383 stations available to build an adequate network for the inversion, so h_{max} is estimated by
384 assuming that both (1) the initial blister shape [i.e. height to radius ratio [$Ar \equiv h_{max}/R =$
385 $O(10^{-3})$] and (2) the ratio of total water volume injected into the ice-bed interface (assumed to
386 be the lake volume) to initial blister volume [$B \equiv V_{tot}/V_i = O(1)$] are the same for all blisters.
387 Thus $V_{tot}/B = V_i = 2\pi\alpha h_{max}R^2 = 2\pi\alpha h_{max}^3/Ar^2 \propto h_{max}^3$, where α is a constant (equation
388 (S.15) in Supplementary Information). We then estimate h_{max} using the known lake volume V_{tot}
389 and the NIF-calculated blister height and lake volume from the 2011 drainage event, h_{max}^{2011}
390 and V_{tot}^{2011} , using $h_{max}/h_{max}^{2011} = (V_{tot}/V_{tot}^{2011})^{1/3}$. The error bar of this h_{max} estimate is
391 propagated from errors in lake volume measurements, as listed in the 4th row of Supplementary
392 Table 2. Note that, even if we consider large variations of constants B and Ar between blisters
393 [i.e., $B = O(0.1 - 10)$ and $Ar = O(10^{-4} - 10^{-2})$], the estimated h_{max} will only vary within
394 one order of magnitude.

395

396 **1.4.3 Blister radius.** Since blister volume is $V_i = 2\pi\alpha R^2 h_{max}$ (see equation (S.15)), the blister
397 radius is estimated via $R = \sqrt{V_i/(2\pi\alpha h_{max})} = \sqrt{V_{tot}/(2\pi\alpha h_{max}B)}$ (estimated blister radii are
398 listed in the table in Fig. 3) and the uncertainty associated with blister radius estimates is related
399 to the uncertainties in estimating V_{tot} and h_{max} (5th row in Supplementary Table 2).

400

401 **1.4.4 Hydraulic transmissivity.** Finally, the errors associated with estimating the transmissivity
402 kh_0 (last row in Supplementary Table 2) is propagated from errors in V_{tot} , h_{max} , and R . The
403 error bar in kh_0 varies from 20% for the 2011 and 2012 drainage events to 40-50% for the 2006
404 and 2009 drainage events, due to larger uncertainties in both measuring lake volume and
405 estimating maximum blister height.

406

407 **1.4.5. Numerical pre-factor f .** One benefit of dimensionless solutions is that the shape of uplift
408 data $h(t)$ for a range of V_{tot} and kh_0 can be compared with the theory on a dimensionless
409 $h/h_i - t/t_c$ plot (Fig. 3c). Theoretically we expect a slight spread of dimensionless data on Fig.
410 3c because the analytical solution of blister height [red curve in Fig. 3c; equation (7)] depends
411 not only on h/h_i and t/t_c but also $f = \alpha \ln[(B - \gamma)/C]$ [equation (S.26) in Supplementary
412 Information]. We estimate that f varies between individual drainage events in the range $f =$
413 $0.5 - 0.8$, as shown in the last row in Supplementary Table 3. In Fig. 3c we plot the solution
414 using the value $f = 0.6$ averaged over all datasets (red dashed curve). The upper and lower
415 bounds of the solutions calculated using $f = 0.5$ and $f = 0.8$, respectively, are illustrated by the
416 black dashed lines in Fig. 3c.

417

418 **1.4.6. Systematic errors.** There are two constants that can cause systematic uncertainties: the
419 Young's modulus of ice ($E \approx 10^{10}$ Pa) and the volume ratio between the lake volume and the
420 initial blister volume ($B \equiv V_{tot}/V_i \approx 1.14$), estimated from the 2012 North Lake volume and the
421 NIF-calculated initial blister volume. Since they cause systematic errors, variations in these
422 parameters will not affect the collapse of the data in Fig. 3c, but will systematically shift the
423 transmissivity value. If we consider an extreme parameter range, $E = O(10^9 - 10^{10})$ Pa and
424 $B = 1 - 5$, the transmissivity $kh_0 \propto R^3/E \propto B^{-3/2}E^{-1}$ will be systematically multiplied by a
425 factor in the range of $0.04 \sim 5$.

426

427 **1.5 Transmissivity Versus Surface Cumulative Runoff**

428 The evolution of basal transmissivity over the course of the melt season is demonstrated in Fig.
429 4a. The x-axis is the transmissivity inferred from the five drainage events in 2006, 2009, 2010,
430 2011, and 2012 among three lakes. The y-axis is the cumulative runoff from the first day of the
431 year in which runoff occurs through the drainage date. The cumulative runoff is calculated from
432 daily 11-km resolution RACMO runoff estimates (27) over the 11-km grid cell at locations of the
433 GPS stations. The Lake F location is 67.01° N 48.74° W (4).

434

435 The difference in cumulative runoff estimates between RACMO (27) and MAR (29) during the
436 late melt season is large and reflected in the vertical error bars. The error bars of the cumulative
437 runoff in Fig. 4a cover the values extrapolated from the regional climate MAR (29) (v3.5.2)
438 model's monthly output averaged from 2006 to 2012 (y-positions of the symbols on the solid
439 blue curve in Fig. 4b).

440

441 **2 Experimental Methods**

442 **2.1 Experimental Setup**

443 We adhered a transparent elastic layer of polydimethylsiloxane (PDMS; Dow Corning Sylgard
444 184 Silicone Elastomer), which mimics ice, to a porous substrate (PDMS micropillar array),
445 which serves as a simple model for the porous drainage system (Fig. 2a), using a double-sided
446 adhesive tape (Drytac). When the fluid (glycerol dyed blue) was injected at the interface of the
447 porous substrate and the adhered elastic layer, it first flowed within the porous substrate, then
448 peeled apart the interface between the two layers, forming a blister. After injecting a total
449 volume V_{tot} of fluid, we observed the time evolution of the fluid in the porous substrate and the
450 blister (Fig. 2b). Darker area indicates a larger blister thickness H , which relaxes with time,
451 forcing a radial fluid flow into the porous substrate. The experimental parameters are listed in
452 Supplementary Table 3. In the experiments the elastic stresses ($\Delta p_e \approx EH/((1 - \nu^2)R) \approx 10^4$
453 Pa) are the driving force for relaxation dynamics since they are much larger than the hydrostatic
454 stresses of the blister fluid ($\rho gH \approx 1$ Pa), similar to the situation of a blister under the ice sheets.

455

456 **2.2 Fabrication of Micropillar Arrays**

457 A porous substrate made of micropillar arrays is used to model the porous drainage system. We
458 designed and fabricated silicon molds for the micropillar arrays using standard photolithography
459 methods. Each mold for the micropillar arrays is 7 cm in diameter and consists of circular wells
460 on a hexagonal array with a porosity of 50%. Three variations of the micropillar array molds
461 were designed with well diameters of 500 μm , 250 μm , and 125 μm and a well depth of 90 μm
462 for each. Polydimethylsiloxane (PDMS) was cast onto the silicon molds using a crosslinker to
463 elastomer ratio of 1 to 5 and cured to create PDMS micropillar arrays.

464

465 **2.3 Permeability Measurement**

466 The permeability of each of the three micropillar arrays of depth $h_0 = 90 \mu\text{m}$ was measured in a
467 $w = 1 \text{ cm}$ wide by $L = 5 \text{ cm}$ long section of the micropillar array bonded to a glass slide. Water
468 was injected into the device using a pressure control pump at a gauge pressure, Δp , and the
469 flowrate, Q , was measured using a digital scale. From Darcy's law, $k = Q\mu L / (wh_0\Delta p)$, we
470 determine the permeability, k , of each micropillar array (listed in Supplementary Table 3).

471

472 **2.4 Blister Volume Measurement**

473 A specified volume of glycerol was injected between the micropillar array and the overlying
474 elastic sheet using a syringe pump. MATLAB was used for image processing to measure the area
475 of the blister and the area of the fluid in the pores. Time $t = 0$ is chosen to be the first image
476 when the area of the blister has stopped increasing. By measuring the area of the fluid in the
477 pores, the volume of fluid in the blister is calculated by subtracting the volume of the fluid in the
478 pores from the total injected volume.

479

480

481 **Data Availability:** GPS Data for North Lake and South Lake are available at the UNAVCO
482 repository (<https://doi.org/10.7283/T55T3J80>, <https://doi.org/10.7283/T58K77VX>,

483 <https://doi.org/10.7283/T54T6H4M>, <https://doi.org/10.7283/T5125RFN>,
484 <https://doi.org/10.7283/T59K4915>). All experimental data reported in this study are available at
485 [LINK TO BE ADDED AFTER REVIEW].

486

487 **Acknowledgements:** C.-Y.L. and L.A.S thank Lamont-Doherty Earth Observatory for funding
488 through the Lamont Postdoctoral Fellowships. D.L.C acknowledges support from the National
489 Science Foundation (NSF) Graduate Research Fellowship. T.T.C. was supported by NSF’s
490 Office of Polar Programs (NSF-OPP) through OPP-1643970, the National Aeronautics and
491 Space Administration (NASA) through NNX16AJ95G, and a grant from the Vetlesen
492 Foundation. S.B.D. and M.D.B. acknowledge funding from NSF-OPP through OPP-1838410
493 and NASA’s Cryospheric Sciences Program through ARC-0520077, ARC-1023364, and
494 NNX10AI30G. H.A.S. thanks the Princeton Environmental Institute and the Carbon Mitigation
495 Initiative at Princeton University.

496

497 **Author Contributions:** All authors contributed to manuscript preparation. C.-Y.L. led the
498 project and the preparation of the manuscript. L.A.S, S.B.D., and M.D.B. supplied GPS uplift
499 data, and with T.T.C. interpreted the result. D.L.C. designed and conducted the experiments, and
500 along with H.A.S. assisted with the model development.

501

502 **Additional information:**

503 **Competing interests** Authors declare no competing interests.

504

505

506

507

508

509

510 **References**

- 511 1. H. J. Zwally, W. Abdalati, T. Herring, K. Larson, J. Saba, K. Steffen, Surface melt-induced
512 acceleration of Greenland ice-sheet flow. *Science*. **297**, 218–222 (2002).
- 513 2. S. B. Das, I. Joughin, M. D. Behn, I. M. Howat, M. A. King, D. Lizarralde, M. P. Bhatia,
514 Fracture Propagation to the Base of the Greenland Ice Sheet During Supraglacial Lake
515 Drainage. *Science*. **320**, 778–781 (2008).
- 516 3. I. Bartholomew, P. Nienow, D. Mair, A. Hubbard, M. A. King, A. Sole, Seasonal evolution
517 of subglacial drainage and acceleration in a Greenland outlet glacier. *Nat. Geosci.* **3**, 408–
518 411 (2010).
- 519 4. S. H. Doyle, A. L. Hubbard, C. F. Dow, G. A. Jones, A. A. W. Fitzpatrick, A. Gusmeroli, B.
520 Kulesa, K. Lindback, R. Pettersson, J. E. Box, Ice tectonic deformation during the rapid in
521 situ drainage of a supraglacial lake on the Greenland Ice Sheet. *The Cryosphere*. **7**, 129–140
522 (2013).
- 523 5. A. J. Tedstone, P. W. Nienow, N. Gourmelen, A. Dehecq, D. Goldberg, E. Hanna, Decadal
524 slowdown of a land-terminating sector of the Greenland Ice Sheet despite warming. *Nature*.
525 **526**, 692–695 (2015).
- 526 6. L. A. Stevens, M. D. Behn, J. J. McGuire, S. B. Das, I. Joughin, T. Herring, D. E. Shean, M.
527 A. King, Greenland supraglacial lake drainages triggered by hydrologically induced basal
528 slip. *Nature*. **525**, 144 (2015).
- 529 7. T. Cowton, P. Nienow, A. Sole, J. Wadham, G. Lis, I. Bartholomew, D. Mair, D. Chandler,
530 Evolution of drainage system morphology at a land-terminating Greenlandic outlet glacier.
531 *Journal of Geophysical Research: Earth Surface*. **118**, 29–41 (2013).
- 532 8. D. M. Chandler, J. L. Wadham, G. P. Lis, T. Cowton, A. Sole, I. Bartholomew, J. Telling,
533 P. Nienow, E. B. Bagshaw, D. Mair, S. Vinen, A. Hubbard, Evolution of the subglacial
534 drainage system beneath the Greenland Ice Sheet revealed by tracers. *Nat. Geosci.* **6**, 195
535 (2013).

- 536 9. C. Schoof, Ice-sheet acceleration driven by melt supply variability. *Nature*. **468**, 803–806
537 (2010).
- 538 10. I. J. Hewitt, Seasonal changes in ice sheet motion due to melt water lubrication. *Earth*
539 *Planet. Sci. Lett.* **371-372**, 16–25 (2013).
- 540 11. C. F. Dow, B. Kulesa, I. C. Rutt, V. C. Tsai, S. Pimentel, S. H. Doyle, D. van As, K.
541 Lindbäck, R. Pettersson, G. A. Jones, A. Hubbard, Modeling of subglacial hydrological
542 development following rapid supraglacial lake drainage. *J Geophys Res Earth Surf.* **120**,
543 1127–1147 (2015).
- 544 12. I. J. Hewitt, Modelling distributed and channelized subglacial drainage: the spacing of
545 channels. *J. Glaciol.* **57**, 302–314 (2011).
- 546 13. V. C. Tsai, J. R. Rice, A model for turbulent hydraulic fracture and application to crack
547 propagation at glacier beds. *Journal of Geophysical Research: Earth Surface.* **115** (2010).
- 548 14. D. R. Hewitt, G. P. Chini, J. A. Neufeld, The influence of a poroelastic till on rapid
549 subglacial flooding and cavity formation. *J. Fluid Mech.* **855**, 1170–1207 (2018).
- 550 15. J. S. Walder, Stability of Sheet Flow of Water Beneath Temperate Glaciers and Implications
551 for Glacier Surging. *J. Glaciol.* **28**, 273–293 (1982).
- 552 16. T. T. Creyts, C. G. Schoof, Drainage through subglacial water sheets. *J. Geophys. Res.* **114**,
553 255 (2009).
- 554 17. J. Weertman, Effect of a Basal Water Layer on the Dimensions of Ice Sheets. *J. Glaciol.* **6**,
555 191–207 (1966).
- 556 18. J. S. Walder, Hydraulics of Subglacial Cavities. *J. Glaciol.* **32**, 439–445 (1986).
- 557 19. B. Kamb, Glacier surge mechanism based on linked cavity configuration of the basal water
558 conduit system. *J. Geophys. Res. [Solid Earth]*. **92**, 9083–9100 (1987).
- 559 20. G. K. C. Clarke, Lumped-element analysis of subglacial hydraulic circuits. *J. Geophys. Res.*
560 *[Solid Earth]*. **101**, 17547–17559 (1996).

- 561 21. C.-Y. Lai, Z. Zheng, E. Dressaire, G. Z. Ramon, H. E. Huppert, H. A. Stone, Elastic
562 Relaxation of Fluid-Driven Cracks and the Resulting Backflow. *Phys. Rev. Lett.* **117**,
563 268001 (2016).
- 564 22. C.-Y. Lai, Z. Zheng, E. Dressaire, H. A. Stone, Fluid-driven cracks in an elastic matrix in
565 the toughness-dominated limit. *Philos. Trans. R. Soc. Lond. A.* **374**, 20150425 (2016).
- 566 23. C.-Y. Lai, B. Rallabandi, A. Perazzo, Z. Zheng, S. E. Smiddy, H. A. Stone, Foam-driven
567 fracture. *Proceedings of the National Academy of Sciences.* **115**, 8082–8086 (2018).
- 568 24. G. E. Flowers, G. K. C. Clarke, A multicomponent coupled model of glacier hydrology 1.
569 Theory and synthetic examples. *J. Geophys. Res. [Solid Earth]*. **107**, ECV–9 (2002).
- 570 27. B. Noël, W. J. van de Berg, E. van Meijgaard, P. Kuipers Munneke, R. S. W. van de Wal,
571 M. R. van den Broeke, Evaluation of the updated regional climate model RACMO2.3:
572 summer snowfall impact on the Greenland Ice Sheet. *The Cryosphere.* **9**, 1831–1844
573 (2015).
- 574 28. I. M. Howat, S. De la Pena, J. H. Van Angelen, J. T. M. Lenaerts, M. R. Van den Broeke,
575 Brief Communication“ Expansion of meltwater lakes on the Greenland ice sheet.” *The*
576 *Cryosphere.* **7**, 201–204 (2013).
- 577 29. X. Fettweis, J. Box, C. Agosta, C. Amory, C. Kittel, C. Lang, D. van As, H. Machguth, H.
578 Gallée, Reconstructions of the 1900–2015 Greenland ice sheet surface mass balance using
579 the regional climate MAR model. *The Cryosphere.* **11**, 1015–1033 (2017).
- 580 30. K. Poinar, I. Joughin, S. B. Das, M. D. Behn, J. T. M. Lenaerts, M. R. Van Den Broeke,
581 Limits to future expansion of surface-melt-enhanced ice flow into the interior of western
582 Greenland. *Geophys. Res. Lett.* **42**, 1800–1807 (2015).
- 583 31. G. Chen, thesis, Massachusetts Institute of Technology (1998).
- 584 32. M. Bevis, J. Wahr, S. A. Khan, F. B. Madsen, A. Brown, M. Willis, E. Kendrick, P.
585 Knudsen, J. E. Box, T. van Dam, D. J. Caccamise 2nd, B. Johns, T. Nylén, R. Abbott, S.
586 White, J. Miner, R. Forsberg, H. Zhou, J. Wang, T. Wilson, D. Bromwich, O. Francis,

- 587 Bedrock displacements in Greenland manifest ice mass variations, climate cycles and
588 climate change. *Proc. Natl. Acad. Sci. U. S. A.* **109**, 11944–11948 (2012).
- 589 33. I. Joughin, S. B. Das, M. A. King, B. E. Smith, I. M. Howat, T. Moon, Seasonal speedup
590 along the western flank of the Greenland Ice Sheet. *Science*. **320**, 781–783 (2008).
- 591 34. L. A. Stevens, M. D. Behn, S. B. Das, I. Joughin, B. P. Y. Noël, M. R. van den Broeke, T.
592 Herring, Greenland Ice Sheet flow response to runoff variability. *Geophys. Res. Lett.* **43**,
593 11–295 (2016).
- 594 35. I. Joughin, S. B. Das, G. E. Flowers, M. D. Behn, R. B. Alley, M. A. King, B. E. Smith, J.
595 L. Bamber, M. R. van den Broeke, J. H. Van Angelen, Influence of ice-sheet geometry and
596 supraglacial lakes on seasonal ice-flow variability. Copernicus Publications on behalf of the
597 European Geosciences Union (2013).
- 598 36. I. M. Howat, A. Negrete, B. Smith, MEaSURES Greenland Ice Mapping Project (GIMP)
599 digital elevation model from GeoEye and WorldView imagery, version 1. Boulder, CO:
600 NASA National Snow and Ice Data Center Distributed Active Archive Center (2017).
- 601 37. I. M. Howat, A. Negrete, B. E. Smith, The Greenland Ice Mapping Project (GIMP) land
602 classification and surface elevation data sets. *The Cryosphere*. **8**, 1509–1518 (2014).
- 603 38. P. Segall, M. Matthews, Time dependent inversion of geodetic data. *J. Geophys. Res.* **102**,
604 22391–22409 (1997).
- 605 39. L. C. Andrews, G. A. Catania, M. J. Hoffman, J. D. Gulley, M. P. Lüthi, C. Ryser, R. L.
606 Hawley, T. A. Neumann, Direct observations of evolving subglacial drainage beneath the
607 Greenland Ice Sheet. *Nature*. **514**, 80–83 (2014).
- 608 40. D. A. Spence, P. Sharp, T. B. Benjamin, Self-similar solutions for elastohydrodynamic
609 cavity flow. *Proc. R. Soc. Lond. A Math. Phys. Sci.* **400**, 289–313 (1985).
- 610 41. M. Morlighem, E. Rignot, J. Mouginot, H. Seroussi, E. Larour, Deeply incised submarine
611 glacial valleys beneath the Greenland ice sheet. *Nature Geoscience*. **7** (2014), 418–422.

- 612 42. R. LeB. Hooke, Flow law for polycrystalline ice in glaciers: Comparison of theoretical
613 predictions, laboratory data, and field measurements. *Rev. Geophys.* **19**, 664 (1981).
- 614 43. I. J. Hewitt, C. Schoof, and M. A. Werder. Flotation and free surface flow in a model for
615 subglacial drainage. Part 2. Channel flow. *J. Fluid Mech.* **702**, 157–187 (2012).
- 616 44. I. Bartholomew, P. Nienow, A. Sole, D. Mair, T. Cowton, S. Palmer, and J. Wadham.
617 Supraglacial forcing of subglacial drainage in the ablation zone of the Greenland ice sheet.
618 *Geophys. Res. Lett.*, **38**, (2011).
- 619 45. T. V. Ball, and J. A. Neufeld. Static and dynamic fluid-driven fracturing of adhered
620 elastica. *Phys. Rev. Fluids.* **3**, 074101 (2018).

Figures

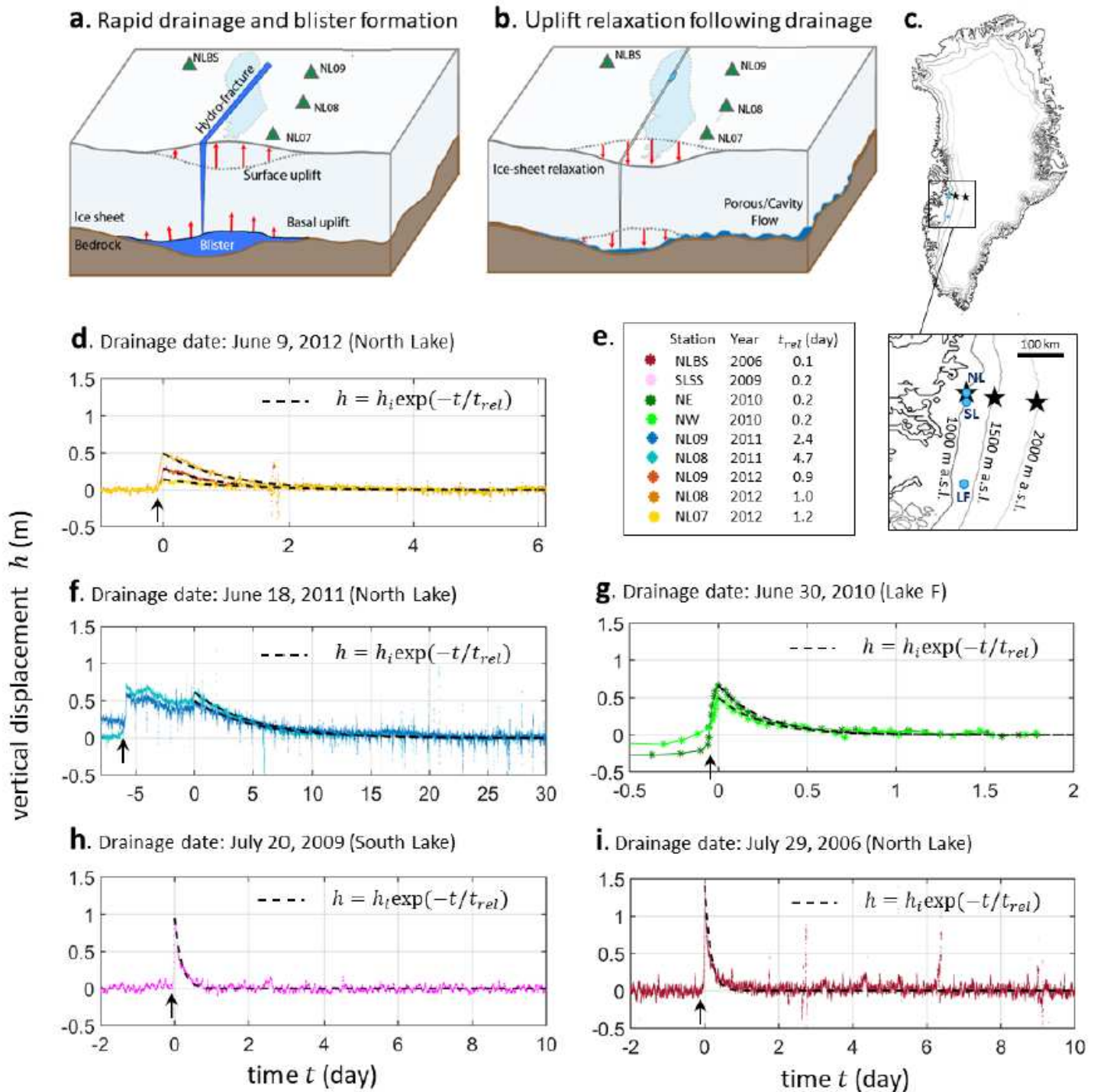


Figure 1

Ice-sheet uplift relaxation following rapid supraglacial lake drainage. Schematic drawings of the North Lake GPS array that observes ice-sheet surface uplift and speed (a) during subglacial blister formation at the time of rapid drainage, and (b) post-drainage relaxation as the blister drains into the surrounding ice-bed interface. (c) The locations of North Lake (NL), South Lake (SL), and Lake F (LF) are marked by the

by equation (6). (d) The dimensionless experimental data fall onto a common curve, agreeing well with the exponential solution (equation (6) with $\beta = 0.6 - 0.7$ (Supplementary Table 3); solid curves).

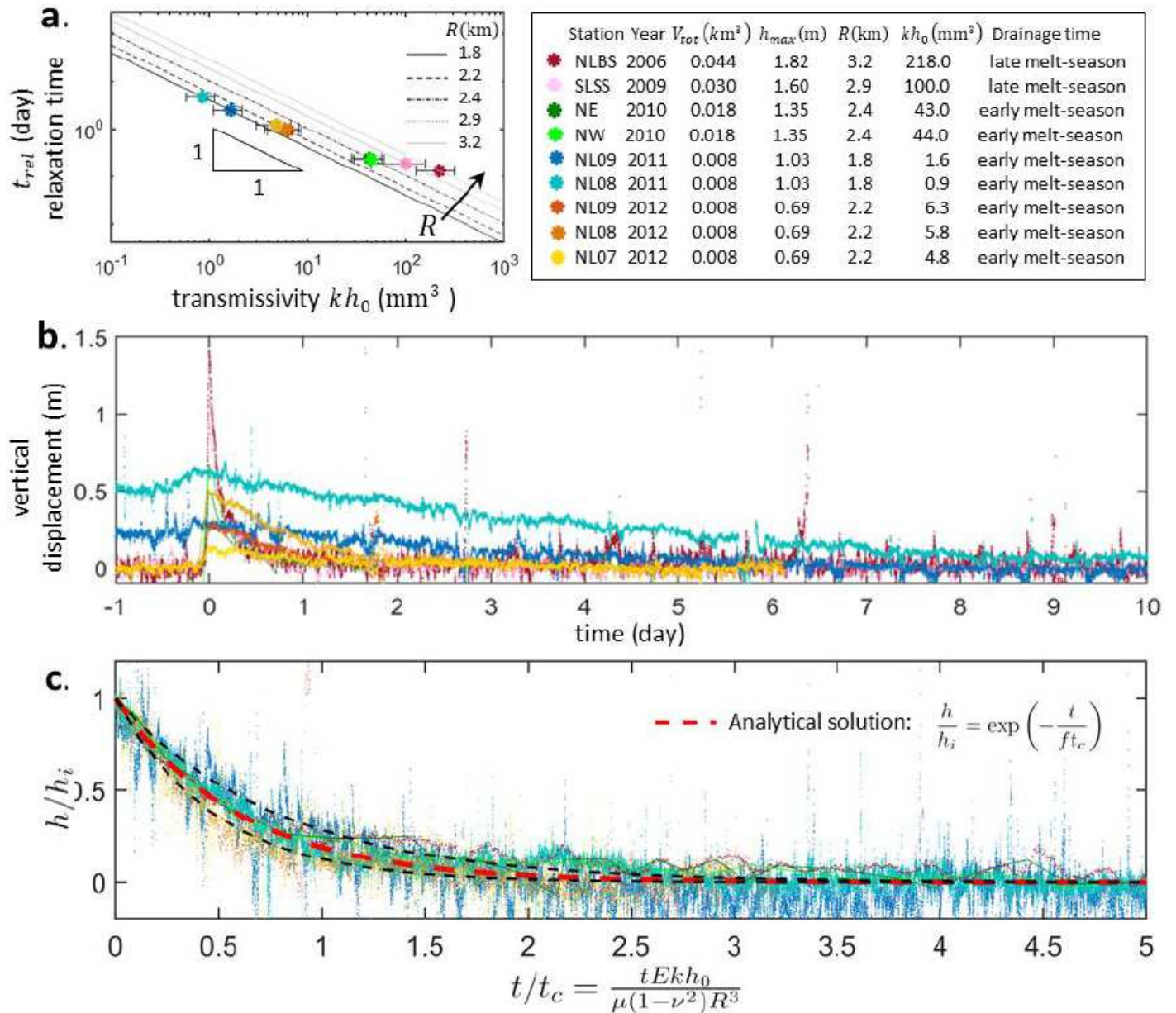


Figure 3

Hydraulic transmissivity and the universal dynamics of uplift relaxation. (a) The relaxation time t_{rel} obtained from surface uplift data from different stations and the predicted hydraulic transmissivity kh_0 . The detailed information for each data set is shown in the table. Here the supraglacial lake volume is assumed to be the total volume V_{tot} injected into the blister and the water sheet. The black lines ($t_{rel} = \frac{R^3}{3(1-\beta^2)(\beta_0-1)}$) are the model predictions for different blister radii R . The lake volume V_{tot} of Lake F and North Lake listed in the table are taken from references (2, 4, 6) and lake volume of South Lake is estimated in Methods. Surface uplift data from five drainages of three different lakes as recorded by seven different stations are plotted in (b) dimensional and (c) dimensionless forms. Despite a wide range

of relaxation times, when rescaled by the characteristic relaxation time τ (equation (4)) and initial vertical displacement δ , all field uplift data collapse onto the exponential analytical solution (equation (7), red dashed line (panel c) with $\tau = 0.6$ averaged over all datasets (Methods)). Upper and lower dashed lines represent the solutions with the highest and lowest τ , respectively, among all the data sets.

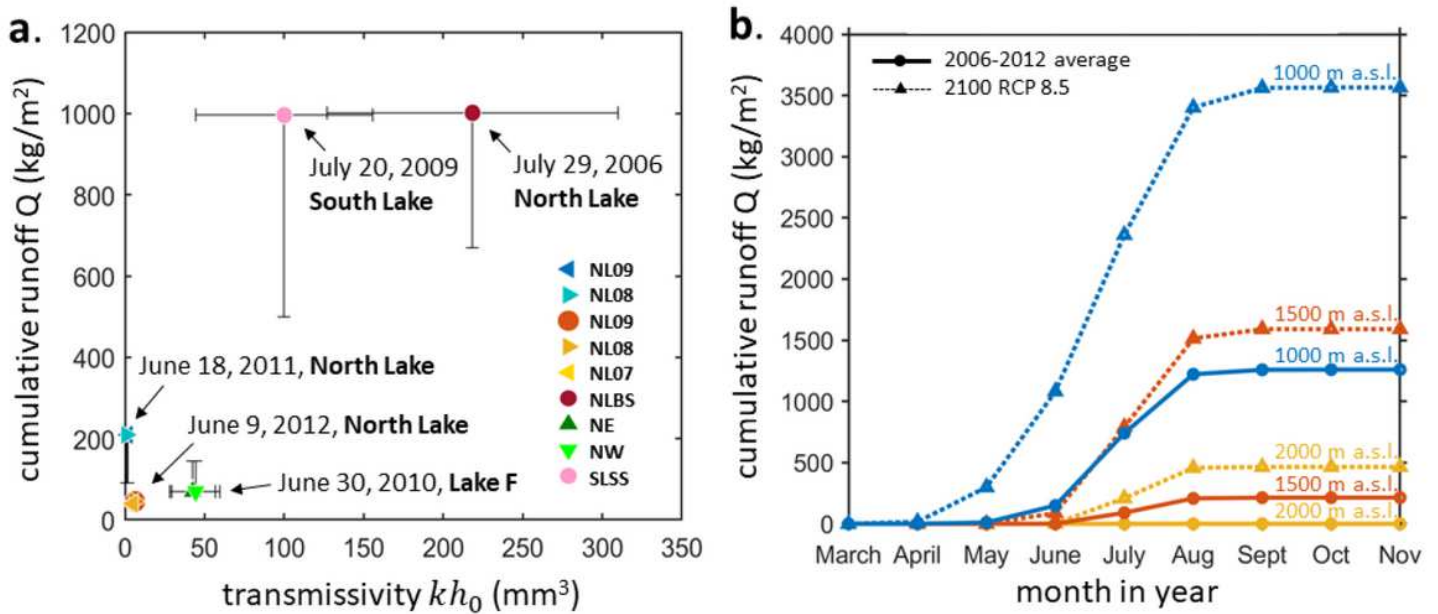


Figure 4

Seasonal variation of hydraulic transmissivity. (a) Transmissivity inferred from five drainage events across three lakes as a function of cumulative runoff. Cumulative runoff is the sum of daily, 11-km resolution RACMO runoff estimates (27) from the first day of the year up to the drainage date at the nearest RACMO grid cell to the drainage location (Methods). (b) Time evolution of cumulative runoff (monthly output) obtained from the regional climate model MAR averaged from 2006 to 2012 (solid curves) and its 2100-projections under the RCP 8.5 scenario (29) (dashed curves), evaluated at the three locations (elevations) marked as stars in Fig. 1c.

Supplementary Files

This is a list of supplementary files associated with this preprint. Click to download.

- [BlisterSI.pdf](#)